Supplementary Information for

Comparison Between Ozone Column Depths and Methane Lifetimes Computed by 1-D and 3-D Models at Different Atmospheric O$_2$ Levels

Aoshuang Ji[*], James F. Kasting[*], Greg Cooke, Daniel Marsh, Kostas Tsigaridis

[*]**Corresponding authors:**
Aoshuang Ji
Department of Geosciences
Penn State University
434 Deike, University Park, PA 16802, USA
Phone: (+1) 814-826-9491
E-mail: azj64@psu.edu

James F. Kasting
Department of Geosciences
Penn State University
435A Deike, University Park, PA 16802, USA
Phone: (+1) 814-865-3207
E-mail: jfk4@psu.edu

This PDF file includes:

> 1-D model descriptions and simulations
> WACCM6 3-D model descriptions and simulations
> Figures S1 to S11
> Tables S1 to S5
> SI References

We here provide more information about calculations performed with the 1-D photochemical model and the WACCM6 3-D model. The 1-D model runs quickly, so we can easily use it to perform sensitivity studies to different model parameters. Some of this information is useful for understanding the story told in the main text. Some of it may be useful to other users of our 1-D model. Note that our model is similar to the photochemical component of the ATMOS model stored on GitHub (https://github.com/VirtualPlanetaryLaboratory/atmos). That is because ATMOS was originally derived from an earlier version of this model. If one wants to calculate vertical temperature profiles self-consistently along with species concentrations, one should use the ATMOS model

rather than the model that we have used here. The 1-D model used in this paper can be found here: https://github.com/AoshuangJi/1-D-photochemical-model.

1. 1-D model
1.1 Ozone column depth comparisons in the 1-D model
We have done a series of experiments with different setups in the 1-D photochemical model and compared the ozone column depth calculations among those (see **Fig. S1**). The 1-D model used here is a descendant of the Segura et al. (2003) model and uses many of the same algorithms, although the photolysis calculations were done differently, as described in more detail below.

1.1.1 Gaussian quadrature for integrating the solar zenith angle globally in the 1-D model
The most significant update in the current 1-D model is the application of Gaussian quadrature to the photolysis subroutine. As briefly discussed in Section 3 of the main text, previous calculations of ozone column depth versus pO_2 by the Kasting group have always been done at a specific solar zenith angle. The preferred solar zenith angle in our most recent paper (Liu et al., 2021) was 48.2^o, for reasons discussed there and in the main text. (This is the insolation-weighted average daytime zenith angle pointed out by Cronin (2014). A diurnal averaging factor of 0.375 is used with this zenith angle to obtain the correct average photon flux.) A single solar zenith angle was a good choice 40 years ago because computers were much slower, and so computational speed was important. But here we wish to compare results with a 3-D model. The 3-D model does calculations at many different solar zenith angles because it includes grid points at different latitudes and tracks diurnal variations. In doing so, it should provide an accurate averaging of solar zenith angles over the entire sunlit hemisphere.

We can obtain accurate, daytime-average photolysis rates in the 1-D model by using Gaussian quadrature. (Technically, we integrate the solar zenith from zero to pi, so the cosine of this angle, μ, goes from 0 to 1. Normal Gaussian integration would be performed over the interval, $-1 \le \mu \le 1$, so we only use half the conventional Gauss points. The sum of the Gaussian weights over the interval 0 to 1 is unity, so the appropriate diurnal averaging factor is 0.5.) By taking increasing numbers of Gauss points on the interval 0-90°, one can refine the integral of incoming sunlight, and the resulting O_2 photolysis rate profile, to arbitrary precision. We have tested the performance of different numbers of Gauss points in calculating the photolysis rate of O_2 at both the middle (60.5 km) and top (99.5 km) of the atmosphere and found that 8 terms (zenith angles 84.55^o, 73.64^o, 62.74^o, 51.84^o, 40.94^o, 30.05^o, 19.17^o, 8.35^o) provided precision to within 0.4% at both altitudes (see **Fig. S2**). A comparison of column-integrated O_2 photolysis rates between the single solar zenith angle of 48.2^o (red dash-dotted straight line) and Gaussian quadrature with different numbers of points are also shown in **Fig. S3**. 8-pt. Gaussian quadrature yields a column-integrated O_2 photolysis rate that is ~3% higher than the single point, 48.2^o, zenith angle model. The 8-Gauss-point model should be closer to the truth here, but the errors in either method are relatively small compared to other uncertainties in the ozone calculation.

The accuracy of the photolysis method is limited by the radiative transfer algorithm employed. We used the Toon et al. (1989) δ 2-stream algorithm with parameters chosen for

solar energy deposition. This method is typically accurate to within a few percent except at high solar zenith angles, where the error is larger. The calculated O_2 photolysis rates include contributions from the Schumann-Runge (SR) bands and the longer-wavelength Herzberg continuum. The shorter-wavelength SR continuum of O_2 is not included in Fig. S3.

In **Fig. S4**, we show comparisons of photolysis rates of O_2 and H_2O calculated using 8-point Gaussian quadrature with those calculated using a single solar zenith angle (48.2° or 60°). Three different atmospheric O_2 levels are shown: 1 PAL, 0.01 PAL and 0.0001 PAL. At lower solar zenith angles (i.e., when the Sun is higher in the sky) the optical depth along a slant path is lower, so UV photons penetrate more deeply into the stratosphere. A solar zenith angle of 48.2° allows deeper UV penetration than one of 60°, so O_2 photolysis rates (JO_2) at low altitudes are greater, increasing ozone production. 8-point Gaussian quadrature allows even deeper UV penetration, further increasing O_2 photolysis rates and ozone production. This method also produced the best agreement with the observed ozone column depth (see **Fig. S1**). So, the 8-point Gaussian quadrature method, along with a diurnal averaging factor of 0.5, was used to perform comparisons with the 3-D model.

In **Fig. S5**, we show comparisons of globally averaged O_2 and H_2O photolysis frequencies calculated by the 1-D model and by WACCM6. The WACCM6 always calculates higher O_2 and H_2O photolysis rates in the troposphere at lower pO_2 levels. Those differences are probably caused by differences in O_2 absorption in the SR bands.

1.1.2 H_2O cross section updates in the 1-D model

Another important update in the 1-D model is the treatment of H_2O photolysis. H_2O absorption cross sections are an integral part of this problem because H_2O photolysis is an important source of the hydroxyl radical, OH. OH participates in catalytic chemistry that destroys ozone, as well as being the primary sink for CH_4. The Kasting model was recently updated to include H_2O absorption cross sections calculated by Ranjan et al. (2020). These become important at lower O_2 levels when solar UV radiation penetrates more deeply into the atmosphere and H_2O photolysis becomes a major source of tropospheric OH. Ranjan et al. extrapolated the H_2O absorption cross sections to 233 nm, revising an older extrapolation (Kasting & Walker, 1981) that cut off at ~210 nm and that evidently underestimated the cross section at that wavelength. (At the time of Kasting and Walker, the measured H_2O cross sections, from Thompson et al. (1963), cut off at 196 nm.) We had anticipated that including these new cross sections would lower the ozone column depth by increasing the rate of H_2O photolysis in the troposphere. To our surprise, however, the ozone column depth actually increased at low pO_2, instead of decreasing. That is because the currently recommended cross sections at shorter wavelengths, from Burkholder et al. (2015), are considerably lower than the Thompson et al. (1963) cross sections which were used in previous Kasting group models. Thus, the rate of H_2O photolysis in the lower troposphere was slower with the new cross sections than it had been previously, and the corresponding ozone column depth was higher (see **Fig. 1** in the main text). For this same reason, revising our H_2O cross sections also increased the lifetime of methane at low pO_2 (see **Table S1**). The original WACCM6 cross sections between 175 - 195 nm were consistent with the Ranjan et al. cross sections, and WACCM6 has now been updated for this study to include the new Ranjan et al. cross sections for wavelengths greater than 195 nm. The ROCKE-3D model does not currently include the new Ranjan et al. H_2O cross sections.

It should be noted that the model from which we started this intercomparison project (from Liu et al., 2021) contained 10 ppmv H_2O in the lower stratosphere, whereas both the WACCM6 and ROCKE-3D models contain half to a third that amount (**Fig. 3** in the main text). (The Segura et al. (2003) model, from which the Liu et al. model was derived, contained 5 or 6 ppmv H_2O in this region, but the temperature profile changed in the newer model, leading to higher H_2O.) The higher H_2O in the older 1-D models results in higher HO_x, which contributes to catalytic loss of ozone. The Segura et al. (2003) model corrected for this problem by using a lower solar zenith angle, 40°. (Indeed, Segura et al. *overcorrected* for this problem because their calculated ozone column depth for the modern atmosphere was higher than the currently accepted value, as discussed in the main text). We corrected this problem by creating a 'low-H_2O' version of the 1-D model that has ~4 ppmv in the lower stratosphere (see Fig. 3 in the main text). In this paper, we refer to that low-H_2O model as the 'standard 1-D model'. The older 1-D model is here referred to as the 'high-H_2O model'. The ozone column depth in the modern atmosphere increased from 287 DU to 298 DU when stratospheric H_2O was lowered (see the comparison of solid curves in **Fig. S1**). Interestingly, lowering H_2O in the 1-D model increased ozone column depths by much more at lower O_2 levels (e.g., by ~50% at 0.001 PAL O_2, see Table 1 in the main text and Fig. S1 here). That's because we dragged H_2O down in the upper troposphere, as well, lowering HO^x abundances and reducing the rate of catalytic ozone destruction.

1.2 Other methodology treatments

1.2.1 Solar UV fluxes

As shown in **Fig. S6**, the solar flux in the 1-D model is larger in the SR continuum (by up to 2.4 times) compared to the two 3-D models. The 1-D model also has a slightly lower flux in the SR bands (by up to 1.15 times), and a slightly higher flux in the Herzberg continuum (by up to 1.2 times). To determine whether the higher shortwave UV solar flux in the 1-D model could be responsible for the discrepancy in the ozone column depths, we repeated the 1-D model calculations using the faruv data (<175 nm) from the WACCM 3-D model. The changes in JO_2 are small for all values of pO_2, especially for the present atmosphere (see **Table S2**). The total JO_2 decreases by about 1% and 12% for 1 PAL and 0.001 PAL O_2, respectively. There is no change in ozone column depth to 3 significant digits when using the new faruv data. WACCM6 calculations with the 1D model solar data show the ozone column may be altered by ~1-4 DU. Thus, we can rule out the different SR continuum fluxes in causing a large proportion of the discrepancies in the ozone column depth.

1.2.2 Lightning effect

Additional methodology concerns that are not discussed in detail in the main text include lightning. In today's atmosphere, lightning is the major non-anthropogenic source of nitrogen oxides in the troposphere (whereas N_2O is the major source of nitrogen oxides in the stratosphere). The 1-D model uses a parameterization developed originally by Chameides and Walker (1981), and then simplified by Kasting (1979) and Kasting et al. (1985). In Kasting et al. (1985), the assumed column-integrated rate of NO production from lightning in the modern atmosphere was 3×10^9 NO molecules $cm^{-2}s^{-1}$, based on observations. The NO production rate

was scaled to lower O_2 levels by assuming thermodynamic equilibrium at a 'freeze-out' temperature of 3500 K in the expanding, cooling, cylindrical shock wave surrounding the lightning bolt. (The freeze-out temperature is the lowest temperature at which kinetic chemical reactions are fast enough to achieve thermodynamic equilibrium as the shock wave passes through an air mass. See **Fig. S7**.) The NO was then distributed with altitude within the troposphere in a manner proportional to the rainout rate, taken from Giorgi and Chameides (1985). We tested the effect on ozone column depth of removing lightning from our model, and it was relatively small: a 7 percent reduction at 1 PAL O_2 and a 7 percent increase at 10^{-4} PAL O_2 (see dotted yellow curve in **Fig. S1**.). Lightning-generated NO produces ozone in the modern troposphere by reacting with odd hydrogen species produced from oxidation of methane and other hydrocarbons. These reactions have been well studied and are important in smog chemistry (Murray, 2016). These effects are too small to account for the difference in ozone column depth between the 1-D and 3-D calculations, but they do affect the concentration of methane and its lifetime in the atmosphere, as explained in Section 5.1 in the main text. We did another simulation with constant NO production at all pO_2 levels, which calculated ~10% higher ozone column depths at pO_2 = 0.1 & 0.01 PAL (see case 16 in Table 1 in the main text). This needs more investigation in our next paper. We compared the CH_4 lifetime between the standard NO parameterization and high NO (production of NO equal to that at present) at 0.1 PAL in the 1-D model and found that the lifetime of CH_4 was reduced by almost a factor of 2 in the high-NO model (**Table S3**). So, this process needs to be taken into account if one hopes to accurately estimate the methane lifetime during the Proterozoic.

Lightning in WACCM6 is parameterised using the Price and Rind (1992) parameterisation, where convective cloud top height influences lightning activity. Lightning emissions of NOx in WACCM6 are compared with other models in Griffiths et al (2021). The effect on clouds from a change of the atmospheric O_2 concentration in WACCM6 is nonlinear, and as a result, so is the effect on NO_x production from lightning. The total NO_x production from lightning in the original C22 simulations is 0.74, 0.75, 0.71, and 0.67 Tg N/yr at 1 PAL, 0.1 PAL, 0.01 PAL, and 0.001 PAL, respectively.

1.2.3 Parameterizations of scattering in the O_2 SR bands

We described the importance of including scattering at O_2 SR band wavelengths in the main text. Here, we provide more detail about how the 1-D model parameterizes this process.

The absorption cross sections for O_2 are critical to calculating ozone column depths because O_2 photolysis produces O atoms, many of which wind up forming ozone. As discussed in the main text, neither the 1-D model nor the two 3-D models do a rigorous job of estimating O_2 cross sections at low O_2 levels. The difficult part of this problem is parameterizing O_2 dissociation in the SR bands (175 – 205 nm). Within this wavelength region, O_2 predissociates, that is, it is excited to a high-energy bound state that then decays into two separate O atoms. Thus, a rotation-vibration spectrum is superimposed on the electronic absorption spectrum.

The straightforward way to calculate the average transmission over a certain wavelength interval is to integrate the monochromatic transmission function over that interval. If the absorption coefficient is k_ν and the pathlength is x, then the integrated transmission function can be written as

$$T(x) = \frac{1}{\upsilon_2 - \upsilon_1} \int_{\upsilon_1}^{\upsilon_2} e^{-k_\upsilon x} d\upsilon \qquad (1)$$

where $[\upsilon_1, \upsilon_2]$ is the spectral interval of interest (Lacis & Oinas, 1991). This procedure can be slow, however, if the absorption coefficient varies rapidly with wavelength, as it does in the SR bands. So, researchers have figured out other ways to do this integration. We discuss two of them here: band models and exponential sums. The discussion that follows applies to the 1-D model.

In all papers published by the Kasting group since 1990, SR band absorption was parameterized following the approach of Allen and Frederick (1982). They published a band model that was based on quantum mechanical calculations by Frederick and Hudson (1980a,b). (In a band model, the average absorption coefficient over each wavelength interval depends on pathlength, as well as on temperature and pressure.) Those calculations, in turn, took advantage of low-pressure, high-resolution laboratory measurements of O_2 absorption by Hudson and Carter (1968). The emphasis in all these studies was on the present atmosphere, for which predissociation of O_2 in the SR bands is a major source of atomic oxygen at altitudes above 60 km. This could lead to errors in the application of these results to low-pO_2 atmospheres because radiation at SR wavelengths would be absorbed in the troposphere, and so shapes of the individual rotation lines would be influenced by pressure broadening more so than by Doppler broadening.

The Allen and Frederick band model is not mathematically suitable for performing calculations involving multiple scattering. (To handle scattering, one needs an absorption coefficient that does not depend on pathlength.) So, scattering is neglected in this, and other, band models. This does not matter much for the present atmosphere because the absorption occurs at high altitudes where the air is thin and Rayleigh scattering is unimportant. But in the low-pO_2 calculations described here and by C22, SR predissociation occurs lower in the atmosphere where scattering is more important. To account for this, coauthor Kasting performed 4-term exponential sum fits to the Allen and Frederick band model that reproduced its behavior in the present atmosphere. (The details of this fitting procedure were described in the Appendix to a paper that was submitted for publication many years ago but which never came out and has since been lost. So, we reiterate the essential elements here.) **Table S4** (Frederick and Hudson, 1980a) lists spectral region of the O_2 Schumann–Runge bands with 500 cm^{-1} intervals. **Table S5** lists the exponential sum coefficients for calculating O_2 absorption in the SR bands which fits to the Allen and Frederick band model in the present atmosphere. With Kasting's exponential sum fits, the transmission function within each wavelength interval can be written as:

$$T(x) = \sum_{i=1}^{N} a_i e^{-k_i x} \qquad (2)$$

A comparison between O_2 photolysis rates calculated for the modern atmosphere using the band model and using the exponential sum fit is shown in Fig. 6 in the main text. Based on visual inspection, the agreement is quite good at all altitudes. From a mathematical standpoint, this parameterization resembles the correlated-k procedure mentioned in the main text, except that the k_i's are calculated in a different manner.

1.2.4 Sensitivity analysis about the chlorine in the 1-D model

Chlorine can destroy O_3 by the well-known catalytic cycle:

$$O_3 + Cl \rightarrow ClO + O_2 \tag{3}$$
$$ClO + O \rightarrow Cl + O_2 \tag{4}$$
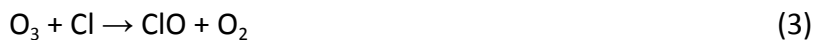
Cl and ClO, collectively, odd chlorine, or ClOx, are produced from the reaction of methyl chloride with the hydroxyl radical or with atomic chlorine

$$CH_3Cl + OH \rightarrow CH_2Cl + H_2O \tag{5}$$
$$CH_3Cl + Cl \rightarrow CH_2Cl + HCl \tag{6}$$
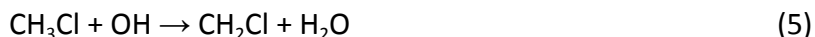
The radical CH_2Cl can then be oxidized by O_2, producing ClO and H_2CO. Methyl chloride is a biogenic gas, like CH_4, and can therefore be modeled in the same way. In the 1-D calculations, we fixed the surface concentration of CH_3Cl at 0.5 ppb for the modern atmosphere. The model calculated an upwards flux of CH_3Cl equal to 2.92×10^8 cm^{-2}s^{-1}, or 3.91 Tg(CH_3Cl)/yr. We then held the CH_3Cl flux constant at this value and performed simulations at lower O_2 levels. Results are shown in Fig. S8-a. The mixing ratio of CH_3Cl peaks at 0.1 PAL of O_2 (for the same reason that the CH_4 mixing ratio peaks there) and decreases to <0.1 ppb at 10^{-4} PAL O_2. The corresponding ozone column depths for this simulation were shown in Fig. 1 and Table 1 in the main text. At 10^{-3} PAL O_2, the column depth was about 30% lower than in the standard run, in which chlorine chemistry was not included. This brings the result closer to the Segura et al. (2003) model, which also included chlorine.

We next performed a similar set of 1-D model runs with a fixed mixing ratio lower boundary condition for CH_3Cl. Results are shown in Fig. S8-b. The drop in column depth is much larger in this case. At 10^{-3} PAL O_2, the column depth decreased from 33 DU to 5 DU, a whopping 85% decrease (compare cases 1 and 10 in Table 1).

Then, in a third experiment (see case 11 in Table 1), we used fixed mixing ratio boundary conditions for CH_3Cl, and we neglected scattering and absorption by CO_2 and H_2O, mimicking what C22 actually did in their WACCM6 calculation. This simulation resulted in nearly a factor of 10 decrease in ozone at 0.01 PAL O_2. At 10^{-3} PAL O_2, the model failed to converge because the chlorine chemistry essentially 'ran away', i.e., the concentrations of Cl-containing species increased to extremely high levels, and ozone decreased to miniscule concentrations. The reason for this behavior is easy to understand: The destruction of CH_3Cl by Cl in reaction (6) is autocatalytic because that destruction leads to still more Cl. To be sure, this did *not* happen in the WACCM6 model, but the potential for instability is clearly present.

2. WACCM6 3-D model
2.1 Brewer-Dobson circulation changes

The Brewer-Dobson circulation is a large-scale atmospheric motion circulation that results in high O_3 abundance in the latitudinal regions where production is relatively low (Brasseur and Solomon 2005). This means that during the northern hemisphere winter, more O_3

is found at northern latitudes than during the summer, despite the fact that less O_3 is produced due to reduced sunlight reaching those latitudes.

The simulations performed by C22 show a reduced amount of O_3 transport to the poles when the O_2 concentration decreases. **Fig. S9** shows the O_3 depth with latitude divided by the global mean O_3 column depth in each simulation. The important point to see is that the peak of the ozone column moves towards the equator when O_2 is reduced, meaning reduced transport of ozone to the poles. This may be due to a reduced amount of O_3 heating in the stratosphere which decreases the temperature contrast between the poles and the equator, but other factors may also be involved.

2.2 Spatial and temporal variability

2.2.1 Latitudinal differences

The time-averaged stratospheric temperature with latitude is illustrated in **Fig. S10** below for 4 different pressures (10 hPa, 50 hPa, 100 hPa, and 200 hPa). The temperature structure is latitudinally asymmetric and the trend with latitude depends on the O_2 concentration. For example, at 10 hPa, for O_2 concentrations above 0.01 PAL, the grid cells in equatorial regions are hotter than the poles. The opposite is true for O_2 concentrations of 0.01 PAL and below. As mentioned previously, differences in temperature affect the reaction rate and number density of molecules, thus affecting the amount of O_3 present in a particular atmospheric grid cell. Combined with transport, seasonal and hemispheric effects will play a role in the abundance and distribution of O_3 across Earth's atmosphere.

2.2.2 Time variability

When comparing a 3D time-variable model which accounts for the diurnal cycle, spatial variability, and seasonal variability, with a time-independent 1D model, it is difficult to quantitatively isolate exactly where discrepancies arise. Comparison of time-averaged and globally averaged profiles from the 3D model with fixed profiles in the 1D model can reveal only limited information.

To give a few examples, during the night in the stratosphere, the lifetime of O_3 is long, whereas in the mesosphere the lifetime is less than an hour (Allen, Lunine, & Yung 1984). At night, NO_2 and O_3 react to create NO_3

$$NO_2 + O_3 \rightarrow NO_3 + O_2 \tag{7}$$

NO_3 exists in low quantities during the day, as it is photolysed easily.

OH and $O(^1D)$, which both act to remove O_3 and CH_4 from the atmosphere, are primarily produced through photolysis during the daytime. At night, their concentrations are several orders of magnitude lower. Importantly, OH is connected to the chemistry of the O_x, HO_x, and NO_x families, and therefore plays both a direct and indirect role in the destruction of O_3 in the atmosphere. The depletion of O_3 and CH_4 is therefore inextricably linked to the diurnal cycle.

Fig. S11 shows that there are stratospheric temperature differences between hemispheres during 4 different months in the WACCM6 model at 1, 0.1, 0.01 and 0.001 PAL.

Generally speaking, the stratospheric difference in temperature between hemispheres decreases when O_2 is lowered.

It is problematic to separate all these 3D and time-variable effects. Several unphysical implementations could be attempted to resolve this obstacle. One could set the obliquity and eccentricity of a 3D model such as WACCM6 or ROCKE-3D to 0, thus removing the seasonal and orbital effects, yet the asymmetry in land and ocean coverage would remain. Additionally, one could tidally lock a 3D model, but at what rotation rate? 1 day, 365 days, or 0? In fact, experiments of this kind have been performed by Proedrou, Hocke, and Wurz (2016) and Proedrou and Hocke (2016), who used a previous version of WACCM6 to investigate the role of tidal locking, as well as sea surface temperatures, on the O_3 abundance and distribution. They used a rotation and orbital period of 365 days. They found the model produced more O_3 on the dayside because of an increased rate of O_x production, and a downwelling on the nightside caused decreased amounts of O_3 on the nightside. Overall, these tidally locked Earth simulations yielded lower globally averaged ozone columns (245 - 250 DU) than the present day Earth simulation (280 DU), showing that horizontal and vertical transport is a significant factor when calculating O_3 columns. Note that a different rotational period choice would alter the atmospheric circulation regime of the tidally locked planet (Carone et al. 2018), thus affecting the O_3 and CH_4 abundance through the transport of chemicals. A single solar zenith angle could be chosen for all grid cells to eliminate the diurnal cycle, but this would alter photolysis rates, heating rates, and again, atmospheric circulation. Moreover, one could impose a single global temperature profile, resulting in no latitudinal or longitudinal dependence on reaction rate, as well as no latitudinal or longitudinal variation in densities, yet this clearly introduces further problems.

2.3 ClO_x and BrO_x catalytic cycles

The WACCM6 simulations include the constituents that comprise the BrO_x and ClO_x chemical families, whereas in this work, the 1D model does not. (Some of the 1-D calculations include chlorine, but none include bromine.) The main source of Cl and Br in WACCM6 is from CH_3Cl and CH_3Br, respectively. The amount of Cl and Br in the stratosphere that is able to destroy O_3 is dependent on photolysis rates and lower boundary conditions. As discussed in the main text, if the surface mixing ratio of CH_3Cl and CH_3Br is kept constant in WACCM6, then the ClO_x and BrO_x catalytic cycles become more important as O_2 decreases. The reactions for Cl with O_3 are the same as reactions (3) & (4). And it is similar for Br with O_3

$$O_3 + Br \rightarrow BrO + O_2, \tag{8}$$
$$BrO + O \rightarrow Br + O_2. \tag{9}$$
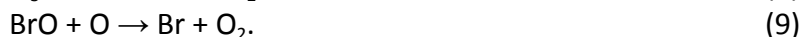
To test the impact of including Cl and Br, in the 0.1 PAL and 0.01 PAL cases in WACCM6, the lower boundary condition of CH_3Cl and CH_3Br were set to be 10 times lower than in the pre-industrial case (in the PI case, the CH_3Br lower boundary mixing ratio was 5.30×10^{-12}, and the CH_3Cl lower boundary mixing ratio was 4.57×10^{-10}). (See Case 17 in Table 1 in the main article). The mean columns in the 0.1 PAL case increased from 169 DU to 180 DU (a change of +6%), and in the 0.01 PAL case from 66 DU to 81 DU (+23%). Thus, inclusion of CH_3Cl and CH_3Br

is important for estimating O_3 column abundances but can only explain ~5-20% of the O_3 column discrepancy between WACCM6 and the 1D model.

But these new 3-D calculations may still have overestimated the flux of methyl chloride. Thus, if we consider extremely low chlorine in the WACCM6, for example, reducing CH_3Cl and all Cl/Br sources by a factor of one billion at the surface (see case 18 in Table 1), i.e., almost 'zero' chlorine in the WACCM6, the average ozone column depth only changes from 81 DU in case 17 to 85 DU in case 18. Compared with the WACCM6 standard run in case 4, however, the zero-chlorine run has about 29% more ozone. By comparison, in the 1-D model, the no-chlorine standard model has about 18% more ozone than the chlorine-containing model at 0.01 PAL O_2. Thus, chlorine has a significant effect on ozone column depth in both models at pO_2 = 0.01 PAL and below. But its effects are amplified in the 1-D model, and chlorine chemistry does not appear capable of explaining the discrepancies at 0.1 PAL O_2.

WACCM6 includes heterogeneous chemistry which is crucial for calculating the depletion of ozone when chlorine is activated on polar stratospheric clouds (PSCs). One of the most important reactions for chlorine destruction in the polar stratosphere is the reaction between HCl and $ClONO_2$ (Solomon et al. 1986). The ozone depletion occurs in spring, when the temperature is still cold enough for PSCs to form and sunlight returns to the pole to activate the chlorine (Brasseur and Solomon 2005). Thus, seasonal effects are required to accurately calculate the ozone loss from the poles.

Realistically, the quantitative importance is unclear due to the unknown fluxes of CH_3Cl and CH_3Br to the atmosphere in the past when O_2 was lower.

References

Allen, M., & Frederick, J. E. (1982). Effective Photodissociation Cross Sections for Molecular Oxygen and Nitric Oxide in the Schumann-Runge Bands. *Journal of the Atmospheric Sciences*, *39*(9), 2066–2075. https://doi.org/10.1175/1520-0469(1982)039<2066:EPCSFM>2.0.CO;2

Allen, M., Lunine, J. I., & Yung, Y. L. (1984). The vertical distribution of ozone in the mesosphere and lower thermosphere. *Journal of Geophysical Research: Atmospheres*, *89*(D3), 4841–4872. https://doi.org/10.1029/JD089iD03p04841

Brasseur, G. P., & Solomon, S. (2005). *Aeronomy of the Middle Atmosphere: Chemistry and Physics of the Stratosphere and Mesosphere* (Vol. 32). Springer Netherlands. https://doi.org/10.1007/1-4020-3824-0

Burkholder, J. B., Sander, S. P., Abbatt, J. P. D., Barker, J. R., Huie, R. E., Kolb, C. E., Kurylo, M. J., Orkin, V. L., Wilmouth, D. M., & Wine, P. H. (2015). Chemical Kinetics and Photochemical Data for Use in Atmospheric Studies: Evaluation number 18. *Pasadena, CA : Jet Propulsion Laboratory, National Aeronautics and Space Administration*, 1392.

Chameides, W. L., & Walker, J. C. G. (1981). Rates of fixation by lightning of carbon and nitrogen in possible primitive atmospheres. *Origins of Life*, *11*(4), 291–302. https://doi.org/10.1007/BF00931483

Carone, L., Keppens, R., Decin, L., & Henning, Th. (2018). Stratosphere circulation on tidally locked ExoEarths. *Monthly Notices of the Royal Astronomical Society*, *473*, 4672–4685. https://doi.org/10.1093/mnras/stx2732

Cronin, T. W. (2014). On the Choice of Average Solar Zenith Angle. *Journal of the Atmospheric Sciences*, *71*(8), 2994–3003. https://doi.org/10.1175/JAS-D-13-0392.1

Frederick, J. E., & Hudson, R. D. (1980a). Atmospheric Opacity. In the Schumann-Runge Bands and the Aeronomic Dissociation of Water Vapor. *Journal of the Atmospheric Sciences*, *37*(5), 1088–1098. https://doi.org/10.1175/1520-0469(1980)037<1088:AOITSR>2.0.CO;2

Frederick, J. E., & Hudson, R. D. (1980b). Dissociation of Molecular Oxygen in the Schumann-Runge Bands. *Journal of the Atmospheric Sciences*, *37*(5), 1099–1106. https://doi.org/10.1175/1520-0469(1980)037<1099:DOMOIT>2.0.CO;2

Giorgi, F., & Chameides, W. L. (1985). The rainout parameterization in a photochemical model. *Journal of Geophysical Research: Atmospheres*, *90*(D5), 7872–7880. https://doi.org/10.1029/JD090iD05p07872

Griffiths, P. T., Murray, L. T., Zeng, G., Shin, Y. M., Abraham, N. L., Archibald, A. T., ... & Zanis, P. (2021). Tropospheric ozone in CMIP6 simulations. *Atmospheric Chemistry and Physics*, *21*(5), 4187-4218. https://doi.org/10.5194/acp-21-4187-2021

Hudson, R. D., & Carter, V. L. (1968). Bandwidth Dependence of Measured uv Absorption Cross Sections of Argon*. *Journal of the Optical Society of America*, *58*(2), 227. https://doi.org/10.1364/JOSA.58.000227

Kasting, J. F. (1979). The evolution of oxygen and ozone in the Earth's atmosphere (Doctoral dissertation, University of Michigan).

Kasting, J. F., Holland, H. D., & Pinto, J. P. (1985). Oxidant abundances in rainwater and the evolution of atmospheric oxygen. *Journal of Geophysical Research: Atmospheres*, *90*(D6), 10497–10510. https://doi.org/10.1029/JD090iD06p10497

Kasting, J. F., & Walker, J. C. G. (1981). Limits on oxygen concentration in the prebiological atmosphere and the rate of abiotic fixation of nitrogen. *Journal of Geophysical Research*, *86*(C2), 1147. https://doi.org/10.1029/JC086iC02p01147

Lacis, A. A., & Oinas, V. (1991). A description of the correlated *k* distribution method for modeling nongray gaseous absorption, thermal emission, and multiple scattering in vertically inhomogeneous atmospheres. *Journal of Geophysical Research*, *96*(D5), 9027. https://doi.org/10.1029/90JD01945

Liu, P., Liu, J., Ji, A., Reinhard, C. T., Planavsky, N. J., Babikov, D., Najjar, R. G., & Kasting, J. F. (2021). Triple oxygen isotope constraints on atmospheric O_2 and biological productivity during the mid-Proterozoic. *Proceedings of the National Academy of Sciences*, *118*(51), e2105074118. https://doi.org/10.1073/pnas.2105074118

Murray, L. T. (2016). Lightning NO x and Impacts on Air Quality. *Current Pollution Reports*, *2*(2), 115–133. https://doi.org/10.1007/s40726-016-0031-7

Price, C., & Rind, D. (1992). A simple lightning parameterization for calculating global lightning distributions. *Journal of Geophysical Research: Atmospheres*, *97*(D9), 9919-9933. https://doi.org/10.1029/92JD00719

Proedrou, E., & Hocke, K. (2016). Characterising the three-dimensional ozone distribution of a tidally locked Earth-like planet. *Earth, Planets and Space*, *68*(1), 96. https://doi.org/10.1186/s40623-016-0461-x

Proedrou, E., Hocke, K., & Wurz, P. (2016). The middle atmospheric circulation of a tidally locked Earth-like planet and the role of the sea surface temperature. *Progress in Earth and Planetary Science*, *3*, 22. https://doi.org/10.1186/s40645-016-0098-1

Ranjan, S., Schwieterman, E. W., Harman, C., Fateev, A., Sousa-Silva, C., Seager, S., & Hu, R. (2020). Photochemistry of Anoxic Abiotic Habitable Planet Atmospheres: Impact of New $H_2 O$ Cross Sections. *The Astrophysical Journal*, *896*(2), 148. https://doi.org/10.3847/1538-4357/ab9363

Segura, A., Krelove, K., Kasting, J. F., Sommerlatt, D., Meadows, V., Crisp, D., Cohen, M., & Mlawer, E. (2003). Ozone Concentrations and Ultraviolet Fluxes on Earth-Like Planets Around Other Stars. *Astrobiology*, *3*(4), 689–708. https://doi.org/10.1089/153110703322736024

Solomon, S., Garcia, R., Rowland, F. *et al.* On the depletion of Antarctic ozone. *Nature* 321, 755–758 (1986). https://doi.org/10.1038/321755a0

Thompson, B. A., Harteck, P., & Reeves, R. R. (1963). Ultraviolet absorption coefficients of CO_2, CO, O_2, H_2O, N_2O, NH_3, NO, SO_2, and CH_4 between 1850 and 4000 A. *Journal of Geophysical Research*, *68*(24), 6431–6436. https://doi.org/10.1029/JZ068i024p06431

Toon, O. B., McKay, C. P., Ackerman, T. P., & Santhanam, K. (1989). Rapid calculation of radiative heating rates and photodissociation rates in inhomogeneous multiple scattering atmospheres. *Journal of Geophysical Research*, *94*(D13), 16287. https://doi.org/10.1029/JD094iD13p16287

Figure captions

Figure S1. O_3 column depths calculated by the 1-D model under different assumptions (all the yellow curves use higher H_2O ~10 ppmv at the cold trap).

Figure S2. Different Gaussian points used for photolysis rates of O_2 at (a) 60.5 km and (b) 99.5 km. These calculations were done for the present atmosphere. The orange dashed straight lines refer to the convergent value for photolysis rates as we include more and more Gaussian points.

Figure S3. Column-integrated photolysis rate of O_2 ($cm^{-2}s^{-1}$) with a single solar zenith angle 48.2° (shown as the red dashed-dotted straight line) and different numbers of Gauss points.

Figure S4. Comparisons of photolysis rates of O_2 and H_2O at varied pO_2 between 8-pt. Gaussian quadrature and a single solar zenith angle. The colors in panel 'b' have the same meaning as in panel 'a'.

Figure S5. Photolysis frequencies of O_2 (panel 'a') and H_2O (panel 'b') in the 1-D model (solid curves) and WACCM6 3D model (dash-dot curves) at different levels of O_2.

Figure S6. Comparisons of the solar flux used in the 1-D, WACCM6 3D and ROCKE-3D models. Note that the solar flux in the 1-D is much higher than those in other two 3D models at the short wavelength region.

Figure S7. Production of NO from lightning as a function of pO_2.

Figure S8. (a) CH_3Cl mixing ratio as a function of pO_2 and (b) CH_3Cl fluxes at varied pO_2 in the 1-D model. The solid green curve in (a) is the standard 1-D run with chlorine chemistry. In (b), the dashed black line represents today's CH_3Cl flux for sustaining 0.5 ppb CH_3Cl in the atmosphere; the solid yellow curve shows fixed 0.5 ppb CH_3Cl as the lower boundary condition; and the solid red curve is fixed 0.5 ppb CH_3Cl plus ignoring the scattering and H_2O/CO_2 in the SR bands. Note that the 1-D model crashed in the latter case at 0.001 PAL.

Figure S9. Normalized O_3 column depths in each pO_2 level at different latitudes in WACCM6 3D model.

Figure S10. Time-averaged stratospheric temperature with latitude (at four different pressures: 10 hPa, 50 hPa, 100 hPa, and 200 hPa) in WACCM6 3D model.

Figure S11. Latitudinally averaged temperature profiles in the Northern hemisphere (NH) and Southern hemisphere (SH) at varied pO_2 levels in the WACCM6 3D model.
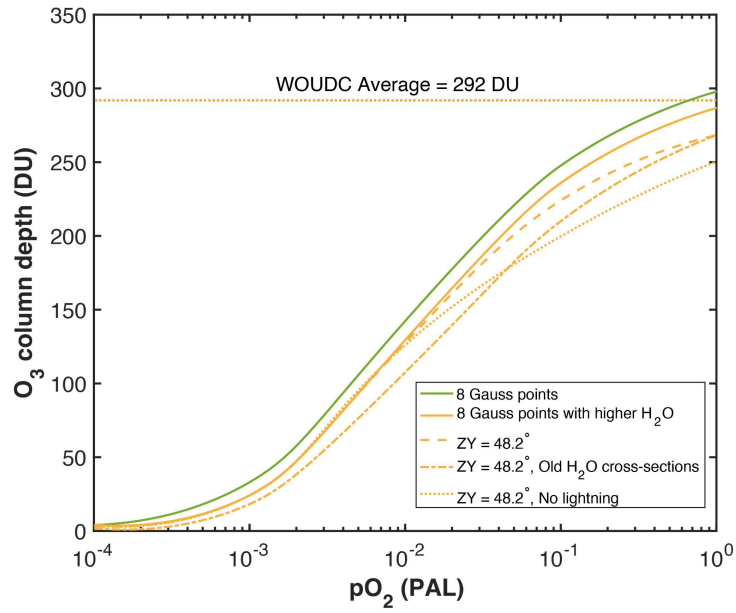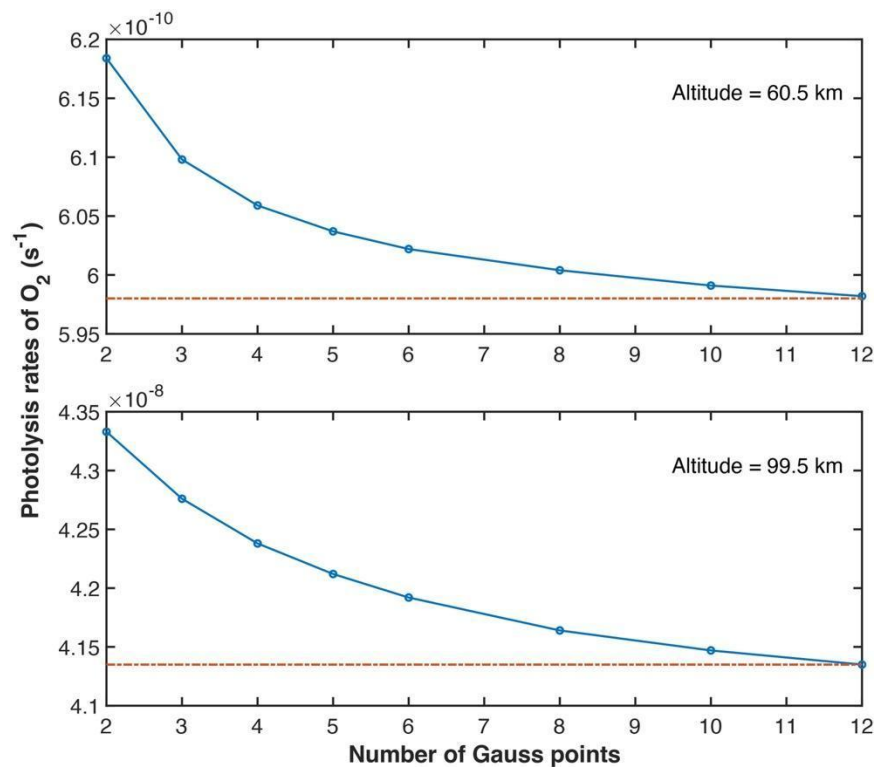
Figure S1. O_3 column depths calculated by the 1-D model under different assumptions (all the yellow curves use higher H_2O ~10 ppmv at the cold trap).

Figure S2. Different Gaussian points used for photolysis rates of O_2 at (a) 60.5 km and (b) 99.5 km. These calculations were done for the present atmosphere. The orange dashed straight lines refer to the convergent value for photolysis rates as we include more and more Gaussian points.
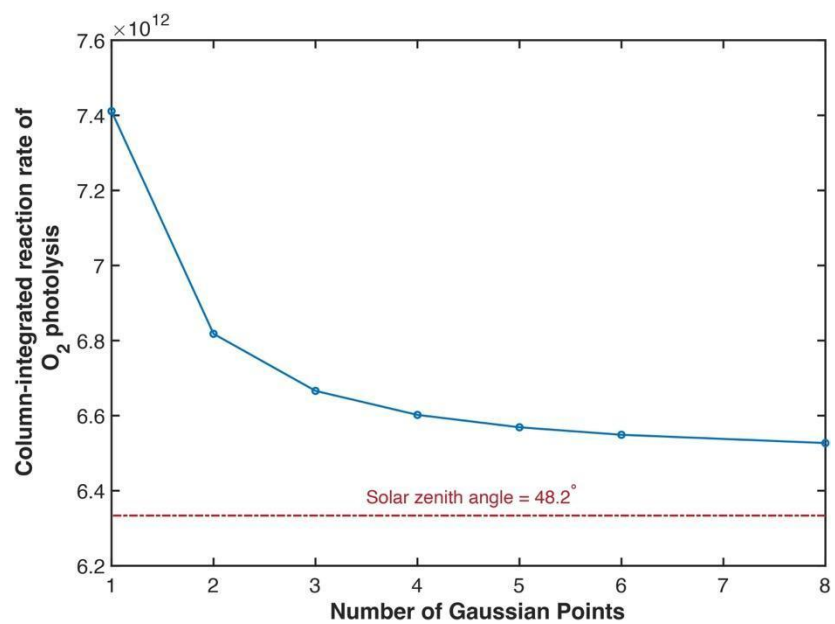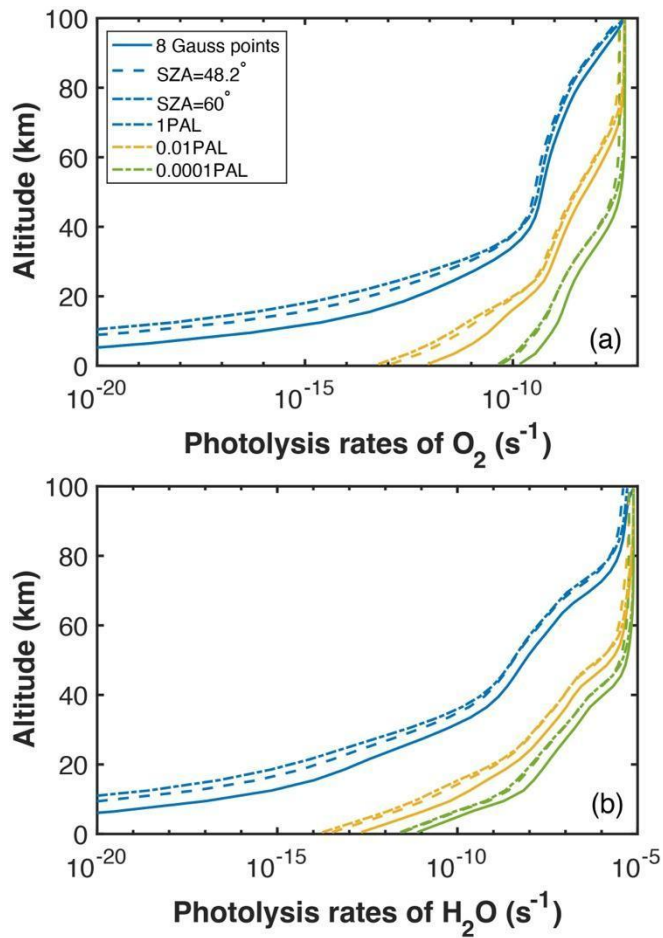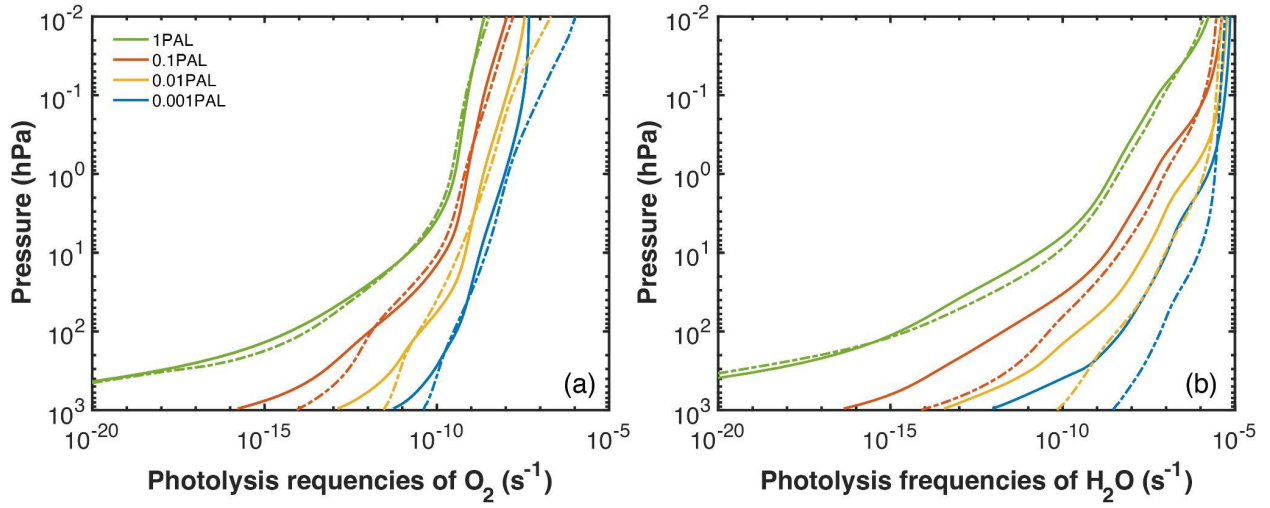
Figure S3. Column-integrated photolysis rate of O_2 (cm^{-2}s^{-1}) with a single solar zenith angle 48.2° (shown as the red dashed-dotted straight line) and different numbers of Gauss points.

Figure S4. Comparisons of photolysis rates of O_2 and H_2O at varied pO_2 between 8-pt. Gaussian quadrature and a single solar zenith angle. The colors in panel 'b' have the same meaning as in panel 'a'.

Figure S5. Photolysis frequencies of O_2 (panel 'a') and H_2O (panel 'b') in the 1-D model (solid curves) and WACCM6 3D model (dash-dot curves) at different levels of O_2.

Figure S6. Comparisons of the solar flux used in the 1-D, WACCM6 3D and ROCKE-3D models. Note that the solar flux in the 1-D is much higher than those in other two 3D models at the short wavelength region.
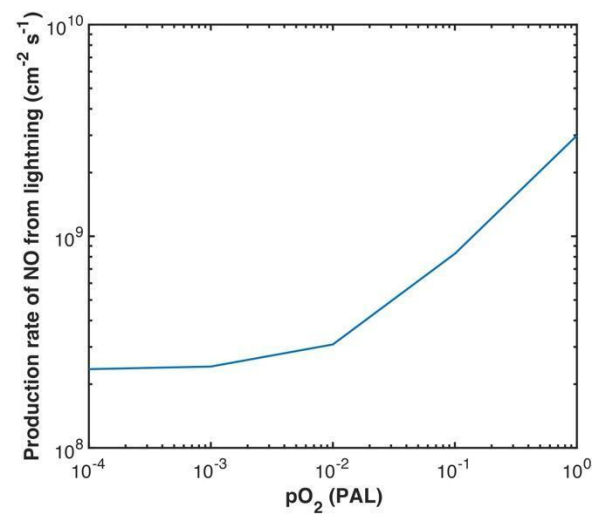
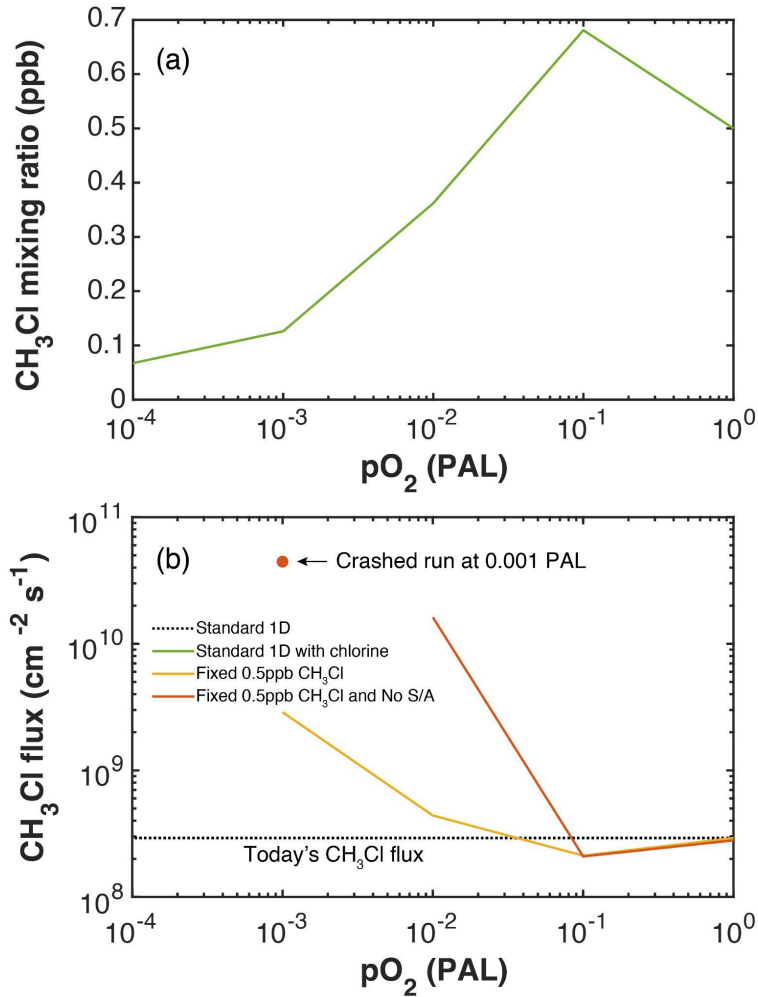**Figure S7.** Production of NO from lightning as a function of pO_2.

Figure S8. (a) CH₃Cl mixing ratio as a function of pO₂ and (b) CH₃Cl fluxes at varied pO₂ in the 1-D model. The solid green curve in (a) is the standard 1-D run with chlorine chemistry. In (b), the dashed black line represents today's CH₃Cl flux for sustaining 0.5 ppb CH₃Cl in the atmosphere; the solid yellow curve shows fixed 0.5 ppb CH₃Cl as the lower boundary condition; and the solid red curve is fixed 0.5 ppb CH₃Cl plus ignoring the scattering and H₂O/CO₂ in the SR bands. Note that the 1-D model crashed in the latter case at 0.001 PAL.
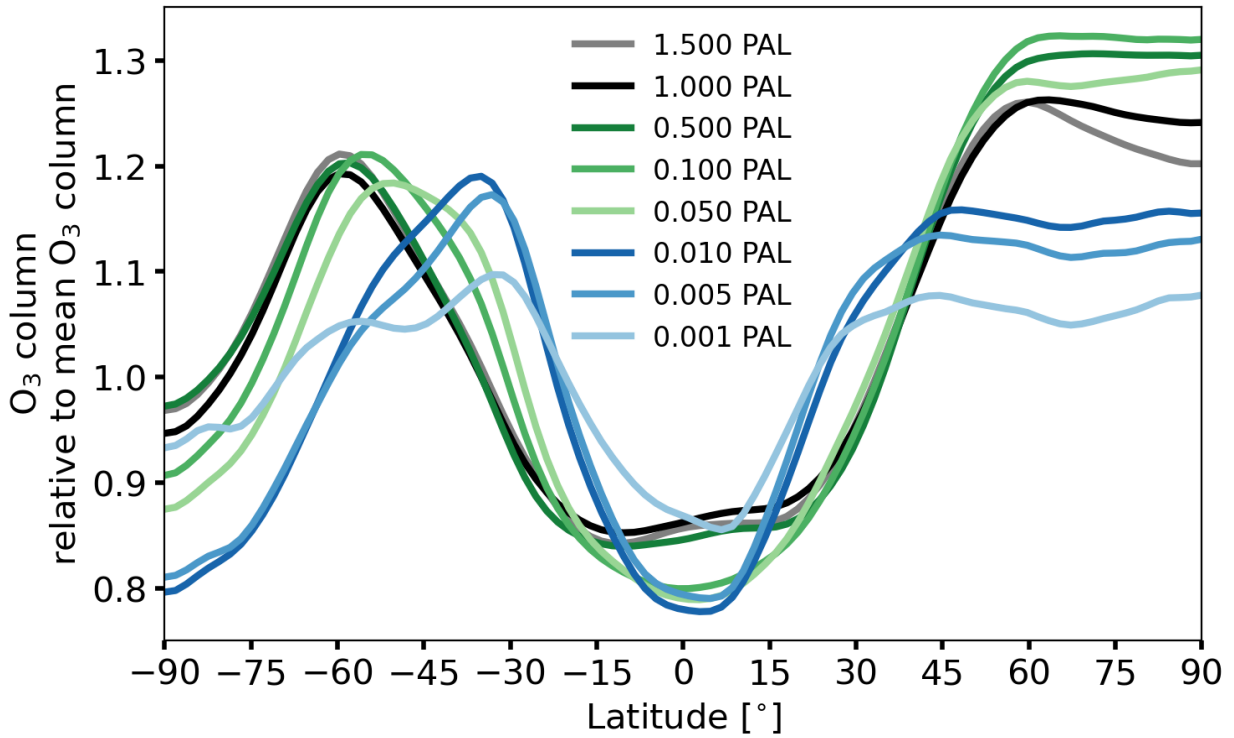
Figure S9. O_3 column depths in each pO_2 level relative to the global mean O_3 column depths at each pO_2 level shown across different latitudes in the WACCM6 3D model. The latitudinal distribution of O_3 changes as pO_2 changes.
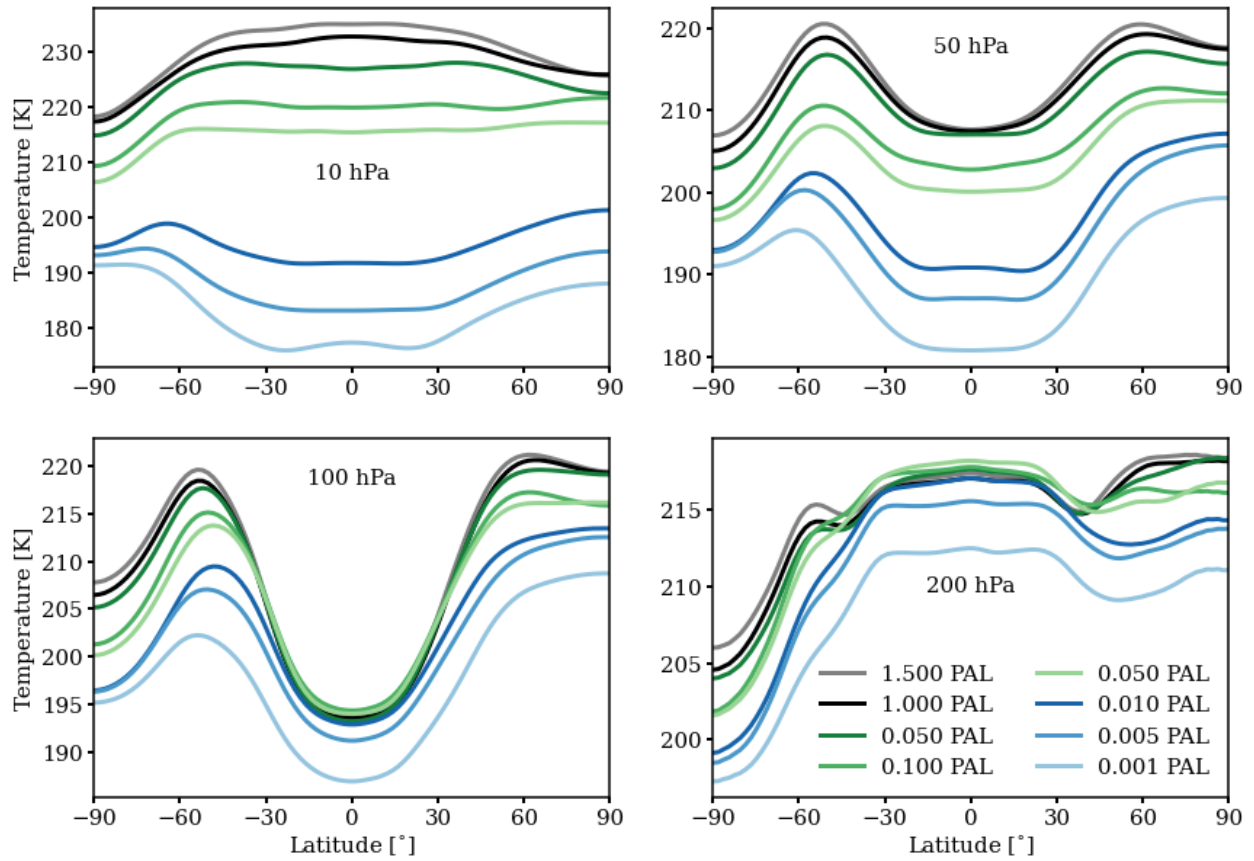
Figure S10. Time-averaged stratospheric temperature with latitude (at four different pressures: 10 hPa, 50 hPa, 100 hPa, and 200 hPa) in WACCM6 3D model.
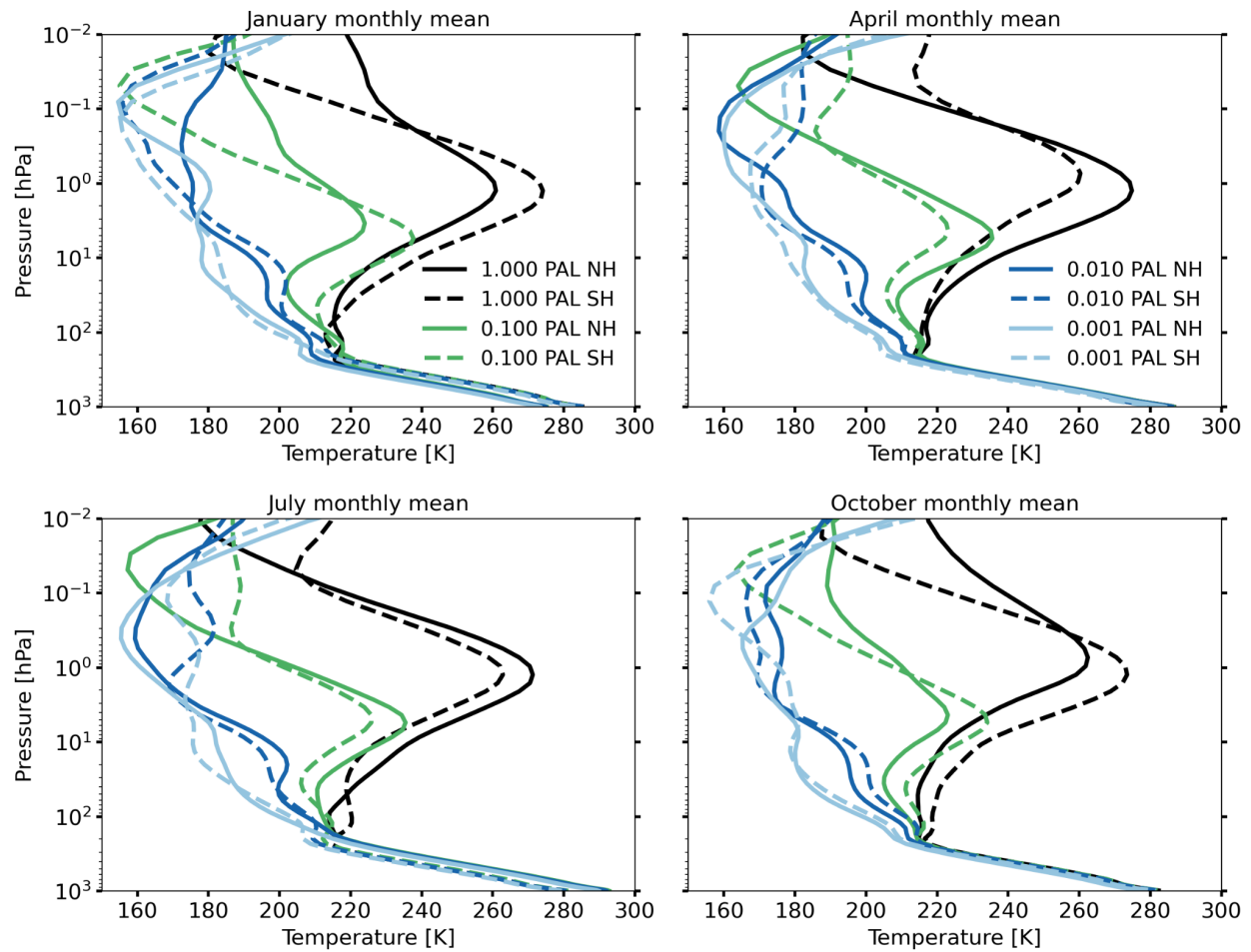
Figure S11. Monthly time-averaged temperature profiles in the Northern hemisphere (NH = 44.53 degrees latitude) and Southern hemisphere (SH = -44.53 degrees latitude) at varied pO$_2$ levels in the WACCM6 3D model. The months of January, April, July, and October are shown.

Table S1. CH_4 lifetime from different calculations as a function of pO_2.

pO_2 (PAL)	1	0.1	0.01	0.001	0.0001
CH_4 lifetime with 8 Gauss points	8.10	13.78	7.35	1.87	0.66
CH_4 lifetime with 8 Gauss points and high-H_2O	7.62	13.3	6.51	1.41	0.54
CH_4 lifetime with 8 Gauss points and no scattering and H_2O/CO_2 absorbers				0.05	
CH_4 lifetime with 8 Gauss points and high eddy diffusion	7.53	8.74	4.62	1.67	
CH_4 lifetime with 48.2 -degree SZA	7.28	12.84	7.05	1.46	0.54
CH_4 lifetime with 8 Gauss points and chlorine	8.00	12.74	5.34	1.36	
CH_4 lifetime with 8 Gauss points and chlorine, no S/A	8.16	12.88	1.64	0.05	
CH_4 lifetime with 8 Gauss points (using 3D temperature profiles for 1% and 0.1% PAL)			9.07	2.65	

Table S2. Column-integrated O_2 photolysis rates ($cm^{-2}\ s^{-1}$).

		1PAL	0.1 PAL	0.01 PAL	0.001 PAL
Column-integrated PO2D	Initial faruv in 1D	1.748×10^{11}	3.822×10^{11}	3.912×10^{11}	3.390×10^{11}
	Apply faruv from 3D into 1D	8.114×10^{10}	1.909×10^{11}	2.082×10^{11}	1.870×10^{11}
Column-integrated PO2	Initial faruv in 1D	6.527×10^{12}	3.095×10^{12}	1.598×10^{12}	8.819×10^{11}
	Apply faruv from 3D into 1D	6.529×10^{12}	3.095×10^{12}	1.596×10^{12}	8.797×10^{11}
Total JO2	Initial faruv in 1D	6.702×10^{12}	3.477×10^{12}	1.989×10^{12}	1.221×10^{12}
	Apply faruv from 3D into 1D	6.610×10^{12}	3.286×10^{12}	1.804×10^{12}	1.069×10^{12}

Table S3. The effect of NO on CH_4 lifetime at 0.1 PAL.

	PNO	nO_3 (surface)	nOH (surface)	$\tau(CH_4)$
Standard	9.853×10^{-3}	2.25×10^{11}	6.65×10^{5}	13.09
High NO	3.574×10^{-2}	3.39×10^{11}	1.38×10^{6}	6.98

Table S4. Spectral region of O_2 Schumann – Runge bands.

Interval I_i	Range of I_i	
	cm^{-1}	nm
1	56500 – 57000	175.4 – 177.7
2	56000 – 56500	177.7 – 178.6
3	55500 – 56000	178.6 – 180.2
4	55000 – 55500	180.2 – 181.8
5	54500 – 55000	181.8 – 183.5
6	54000 – 54500	183.5 – 185.2
7	53500 – 54000	185.2 – 186.9
8	53000 – 53500	186.9 – 188.7
9	52500 – 53000	188.7 – 190.5
10	52000 – 52500	190.5 – 192.3
11	51500 – 52000	192.3 – 194.2
12	51000 – 51500	194.2 – 196.1
13	50500 – 51000	196.1 – 198.0
14	50000 – 50500	198.0 – 200.0
15	49500 – 50000	200.0 – 202.0
16	49000 – 49500	202.0 – 204.1
17	48500 – 49000	204.1 – 206.2

Table S5. Exponential sum coefficients for O_2 in the SR bands. 'N' is the number of non-zero terms in each wavelength interval.

l_i	N	A1	A2	A3	A4
		K1	K2	K3	K4
1	3	0.26360	0.47208	0.26432	0.00000
		2.1549E-20	1.0201E-19	5.0956E-19	0.0000E+00
2	4	0.37394	0.32727	0.17924	0.11955
		3.1815E-21	1.4877E-20	9.6350E-20	7.6965E-19
3	4	0.54935	0.19950	0.16324	0.08790
		1.8008E-21	8.6368E-21	5.0848E-20	3.0440E-19
4	4	0.34674	0.29605	0.22814	0.12907
		1.4823E-21	6.5329E-21	4.2558E-20	2.7521E-19
5	3	0.51000	0.30872	0.18128	0.00000
		8.1948E-22	7.0062E-21	1.1333E-19	0.0000E+00
6	3	0.42433	0.41256	0.16311	0.00000
		3.7925E-22	2.8431E-21	3.8916E-20	0.0000E+00
7	4	0.33693	0.40358	0.19907	0.06042
		2.3694E-22	1.0478E-21	6.5329E-21	6.6572E-20
8	4	0.38154	0.39166	0.17958	0.04723
		9.7031E-23	4.8461E-22	3.2138E-21	3.0968E-20
9	4	0.60810	0.30851	0.05580	0.02759
		7.6886E-23	6.0066E-22	6.0754E-21	2.1072E-20
10	4	0.68739	0.22851	0.06887	0.01523
		7.0630E-23	6.7364E-22	5.5949E-22	2.0992E-20
11	3	0.41084	0.43140	0.15776	0.00000
		4.3962E-23	2.5010E-22	2.0060E-21	0.0000E+00
12	2	0.72673	0.27327	0.00000	0.00000
		3.7391E-23	3.0696E-22	0.0000E+00	0.0000E+00
13	2	0.86499	0.13501	0.00000	0.00000
		2.6937E-23	1.6078E-22	0.0000E+00	0.0000E+00
14	3	0.90156	0.08761	0.01082	0.00000
		2.2109E-23	6.3908E-23	4.8883E-23	0.0000E+00
15	2	0.68851	0.31149	0.00000	0.00000
		2.0184E-23	2.6244E-23	0.0000E+00	0.0000E+00
16	2	0.21803	0.78197	0.00000	0.00000
		1.8368E-23	2.1153E-23	0.0000E+00	0.0000E+00
17	1	1.00000	0.00000	0.00000	0.00000
		1.9572E-23	0.0000E+00	0.0000E+00	0.0000E+00